Spherical versus elongated particles – Numerical investigation of mixing characteristics in a gas fluidized bed

Mema, Ivan; Padding, Johan T.

DOI
10.1016/j.cesx.2020.100079

Publication date
2020

Document Version
Final published version

Published in
Chemical Engineering Science: X

Citation (APA)
Mema, I., & Padding, J. T. (2020). Spherical versus elongated particles – Numerical investigation of mixing characteristics in a gas fluidized bed. *Chemical Engineering Science: X*, *8*, Article 100079. https://doi.org/10.1016/j.cesx.2020.100079

Chemical Engineering Science: X 8 (2020) 100079

Contents lists available at ScienceDirect

Chemical Engineering Science: X

journal homepage: www.elsevier.com/locate/cesx

Spherical versus elongated particles – Numerical investigation of mixing characteristics in a gas fluidized bed

Ivan Mema *, Johan T. Padding

Complex Fluid Processing, Department of Process and Energy, Delft University of Technology, Leeghwaterstraat 39, 2628 CB Delft, the Netherlands

ARTICLE INFO

Article history:
Received 20 May 2020
Received in revised form 21 August 2020
Accepted 11 September 2020

Keywords:
Fluidized bed
Non-spherical particles
Mixing
CFD-DEM
Geldart D

ABSTRACT

The possibility to offer good intermixing between particles is one of the main properties that make fluidized beds such an important industrial appliance. In this work, we use CFD-DEM simulations to compare mixing characteristics of spherical (AR-1) to elongated spherocylindrical particles (AR-4) of aspect ratio In simulation of AR-4 particles, single-particle and multi-particle correlations for hydrodynamic forces are tested. The results show that elongated particles have more vigorous intermixing and lower mixing times compared to spherical particles. Multi-particle correlations have a slight effect on particle mixing, and they increase the difference between AR-1 and AR-4 particles at higher gas velocities. Including hydrodynamic lift force and torque in the case of AR-4 particles leads to more vigorous mixing and lower mixing times.

1. Introduction

In industry many processes rely on manipulation of solid granular materials suspended by a gas, such as gasification, drying, coating, food processing and gas phase polymerization. For this kind of application fluidized beds are irreplaceable equipment, offering high levels of contact between gas and solids together with high levels of intermixing between particles. The mechanism of particle mixing in fluidized bed is closely related to the bubble formation and motion (Kunii, 2013; Rowe and Nienow, 1976; Oschmann et al., 2014).

Being such an important parameter for fluidization, the mixing characteristics of spherical particles, mostly A and B powders, have been subject of many numerical and experimental studies and are generally well understood (Rowe and Nienow, 1976; Thiel and Potter, 1978; Shi and Fan, 1984; Peeler and Huang, 1989; Shen et al., 1995; Rhodes et al., 2001; Deen et al., 2010; Banaei et al., 2018). Because many industrial processes use particles of non-spherical shape, recent years have witnessed an increase in development of numerical models for simulation of fluidized beds with non-spherical particles (Lu et al., 2015; Zhong et al., 2016; Vollmari et al., 2016; Mahajan et al., 2018a). Fluidization behavior of such particles is still not well understood, especially when it comes to fluidization in three dimensional (3D) fluidized beds. In our previous work we showed that elongated particles behave considerably different from spherical ones when suspended in gas flow (Mema et al., 2019; Mema et al., 2019; Mema et al., 2020) as they experience different particle–particle interactions together with additional hydrodynamic forces. Therefore findings that apply to spherical particles cannot be automatically assumed to be valid for elongated ones. So far, the only investigation that looked into mixing characteristics of non-spherical particles was done by Oschmann et al. (2014). Their work was the first that indicated a difference in mixing behavior between spherical particles and non-spherical particles of different aspect ratios. However, the exact cause of this different mixing behavior is not yet understood and needs more extensive research. Their work also did not take into account effects of lift force and hydrodynamic torque, both of which have proven to be important for accurately predicting the behavior of elongated particles in fluidized beds (Mema et al., 2019). Recently, Sanjeevi and Padding (2020) developed multi-particle correlations for drag and lift force and hydrodynamic torque for elongated particles of aspect ratio 4. These correlations take into account the effect of surrounding particles the so-called crowding effect on hydrodynamic forces and torque experienced by the particles. It is known that using multi-particle correlations leads to better predictions of the particles average orientation and average velocity in z-direction (Mema and Padding, 2020), however their effect on particle mixing is still not investigated.

In this work, we apply the computational fluid dynamics, coupled with a discrete element model (CFD-DEM), which was used and validated in previous works (Mahajan et al., 2018a; Mema and Padding, 2020), to compare mixing characteristics of spherical

---

* Corresponding author.
E-mail address: I.Mema@tudelft.nl (I. Mema).

https://doi.org/10.1016/j.cesx.2020.100079
2590-1400/

aspect ratio 1 (AR-1) particles to elongated, spherocylindrical particles of aspect ratio 4 (AR-4) for different gas excess velocities. We also investigate the effect of multi-particle correlations for hydrodynamic forces and torque and show the importance of the effects of lift force and hydrodynamic torque on the mixing properties of elongated (AR-4) particles.

2. Numerical model

For this study, we used a CFD-DEM algorithm based on open source CFDEM coupling (Kloss et al., 2012). This package couples two open source softwares, OpenFOAM which uses a CFD solver to solve the fluid equations and LIGGGHTS which solves particle equations using a discrete element method (DEM). These codes have been adapted so that they can deal with spherocylinders, without relying on a multi-sphere approach. More information about the model and its validation can be found in previous works (Mahajan et al., 2018a; Mema et al., 2019).

2.1. Discrete Element Model (DEM)

To simulate interactions between solid particles we have applied the discrete element model (DEM), a soft contact model first introduced by Cundall and Strack (1979) to describe interaction between granular particles. In this model trajectory of each particle is numerically integrated over time, subject to local forces and torques. The translational motion for particle i can be calculated by integrating the expression

$$m_i \frac{d\mathbf{v}_i}{dt} = \sum_j (\mathbf{F}_{ij,n} + \mathbf{F}_{ij,t}) + \mathbf{F}_{i,f} + \mathbf{F}_{i,p} + \mathbf{F}_{i,b} \tag{1}$$

where the sum runs over all neighbours j in contact with particle i, $\mathbf{F}_{ij,n}$ is the normal contact force acting on particle i due to its interaction with particle j, $\mathbf{F}_{ij,t}$ is the tangential contact force acting on on particle i due to its interaction with particle j, $\mathbf{F}_{i,f}$ is the total hydrodynamic force acting on the particle, $\mathbf{F}_{i,p}$ represents the pressure gradient (buoyancy) force acting on the particle and $\mathbf{F}_{i,b}$ is any body force acting on the particle including gravity. The rotational motion of a particle i can be solved using

$$\frac{d(\mathbf{I}_i \cdot \boldsymbol{\omega}_i)}{dt} = \sum_j \mathbf{T}_{ij} + \mathbf{T}_{i,f} \tag{2}$$

where $\mathbf{I}_i$ is the particle moment of inertia tensor, $\boldsymbol{\omega}_i$ is the angular velocity of the particle, $\mathbf{T}_{ij}$ is the contact torque acting on the particle i due to its interaction with neighbouring particle j, and $\mathbf{T}_{i,f}$ is the fluid-induced pitching torque. Note that for spherical particles, the contact torque $\mathbf{T}_{ij}$ is only caused by tangential contact forces. However, for non-spherical particles the torque is caused by *both* tangential and normal contact forces.

Inter-particle forces develop only when particles spatially overlap. Two adjacent spherical particles are overlapping when the distance between their centers is smaller than the sum of their radii. Calculating overlap in the case of spherocylindrical particles is more complicated as it requires the distance between their shafts to be smaller then sum of their radii. An algorithm for calculating the shortest distance between shafts is presented by Vega and Lago (1994), and more detailed information about its application in the used model can be found in Mahajan et al. (2018a), Mema et al. (2019).

To calculate the normal contact force exerted on particle P_1 by particle P_2 we use a linear spring-dashpot model such that the normal contact force is given by

$$\mathbf{F}_{12,n} = -k_n \delta_n \boldsymbol{n}_{12} - \eta_n \mathbf{v}_{12,n} \tag{3}$$

where k_n is the normal spring constant, η_n is the normal damping coefficient and $\mathbf{v}_{12,n}$ is the normal relative velocity between the particles. As shown in Eq. (3), the normal contact force is dependent on the degree of overlapping distance δ_n, which is calculated with the aforementioned collision detection scheme for spherocylinders.

The magnitude of the tangential contact force is calculated from the Coulomb-type friction expression

$$\mathbf{F}_{12,t} = \begin{cases} -k_t \boldsymbol{\delta}_t - \eta_t \mathbf{v}_{12,t} & \text{if } |\mathbf{F}_{12,t}| \leqslant \mu |\mathbf{F}_{12,n}| \\ -\mu |\mathbf{F}_{12,n}| \boldsymbol{t}_{12} & \text{if } |\mathbf{F}_{12,t}| > \mu |\mathbf{F}_{12,n}| \end{cases} \tag{4}$$

In this expression $\boldsymbol{t}_{12}$ is tangential unit vector defined as $\boldsymbol{t}_{12} = \mathbf{v}_{12}/|\mathbf{v}_{12}|, k_t, \boldsymbol{\delta}_t, \eta_t, \mu$ and $\mathbf{v}_{12,t}$ are the tangential spring constant, tangential overlap, tangential damping coefficient, friction coefficient and tangential relative velocity respectively. $\boldsymbol{\delta}_t$ is calculated from the time integral of the tangential relative velocity since the development of the initial particle contact and given by

$$\boldsymbol{\delta}_t = \int_{t_{c,0}}^{t} \mathbf{v}_{12,t} dt \tag{5}$$

where $t_{c,0}$ is the time of initial contact between the particles.

2.2. Computational Fluid Dynamics (CFD)

In CFD-DEM the fluid phase is treated as a continuum, and is described on the basis of the volume-averaged Navier–Stokes equations, which are discretised on a uniform grid. The equation of continuity and momentum conservation are given by

$$\frac{\partial\left(\epsilon_f \rho_f\right)}{\partial t} + \nabla \cdot \left(\epsilon_f \rho_f \mathbf{v}_f\right) = 0 \tag{6}$$

$$\frac{\partial\left(\epsilon_f \rho_f \mathbf{v}_f\right)}{\partial t} + \nabla \cdot \left(\epsilon_f \rho_f \mathbf{v}_f \mathbf{v}_f\right) = -\epsilon_f \nabla p + \nabla \cdot \left(\epsilon_f \boldsymbol{\tau}_f\right) + \mathbf{R}_{f,p} + \epsilon_f \rho_f \mathbf{g} \tag{7}$$

where ϵ_f is the fluid volume fraction, ρ_f is the fluid density, $\mathbf{v}_f$ is the fluid velocity, $\boldsymbol{\tau}_f$ is the stress tensor for the fluid phase, $\mathbf{g}$ is gravity, and $\mathbf{R}_{f,p}$ represents the momentum exchange between the fluid and particle phase, expressed as:

$$\mathbf{R}_{f,p} = -\frac{\sum_{p=1}^{N_p} (\mathbf{F}_D^p + \mathbf{F}_L^p)}{V_{\text{cell}}} \tag{8}$$

where p is the particle label, N_p is the number of particles in the computational fluid cell, $\mathbf{F}_D^p$ is the drag force acting on particle p due to the fluid, $\mathbf{F}_L^p$ is the lift force acting on particle p due to the fluid, and V_{cell} is the volume of the computational fluid cell. We do not consider two-way coupling of the torque since it has a negligible localized effect on the fluid.

2.2.1. Hydrodynamic forces

The interaction between the fluid phase and solid particles is resolved trough closures for hydrodynamic forces. The main driving force for fluidization is the drag force and it is considered for both AR-1 and AR-4 particles, while lift force and hydrodynamic torque are considered only for AR-4 particles. For calculating hydrodynamic forces in case of AR-4 particles we applied two approaches: with single particle correlations and with multi-particle correlations. Correlations applied in different cases explored in this work are listed in Table 1.

Drag force. *Single-particle drag correlation* In the case of AR-1 particles and AR-4 particles with single-particle correlations, the

Table 1
Correlations for hydrodynamic forces applied in this study.

	AR-1	AR-4	
		Single-particle	*Multi-particle*
Drag	Hölzer and Sommerfeld (2008)	Hölzer and Sommerfeld (2008)	Sanjeevi and Padding (2020)
Lift	-	Zastawny et al. (2012)	Sanjeevi and Padding (2020)
Torque	-	Zastawny et al. (2012)	Sanjeevi and Padding (2020)

drag force experienced by a particle is calculated using Felice's (1994) modified drag force expression:

$$\mathbf{F}_D = \frac{1}{2} C_D \rho_f \epsilon_f^{2-\chi} \frac{\pi}{4} d_p^2 |\mathbf{v}_f - \mathbf{v}_i| (\mathbf{v}_f - \mathbf{v}_i) \tag{9}$$

where $\mathbf{v}_f$ is the fluid velocity interpolated to the location of particle i, C_D is the drag force coefficient, d_p the volume-equivalent particle diameter, $\mathbf{v}_i$ is the velocity of particle i and χ is the Di Felice correction factor given by

$$\chi = 3.7 - 0.65 \exp\left[\left(-(1.5 - \log(\mathrm{Re}))^2/2\right]\right. \tag{10}$$

where the particle Reynolds number Re is calculated as $\mathrm{Re} = \rho_f d_p |\mathbf{v}_f - \mathbf{v}_i| / \mu_f$ with ρ_f being the fluid density and μ_f the fluid viscosity. The Di Felice drag force expression was developed to take into account the effect of surrounding particle (crowding effect) on the drag force experienced by a particle. Even though it was originally developed for spherical particles, the Di Felice expression continued to be applied in simulations of elongated particles fluidization (Oschmann et al., 2014; Vollmari et al., 2016; Mahajan et al., 2018a; Ma and Zhao, 2018; Shrestha et al., 2020) because it was until recently the only option for approximating the crowding effect. Comparison between the effects of the Di Felice approximation and a few other more recently developed models for approximating the crowding effect on drag force can be found in work by Mahajan et al. (2018a).

Even though the Di Felice expression was applied, because the drag force coefficient is calculated using the single particle, Hölzer and Sommerfeld (2008) correlation, simulations with AR-4 particles done using this approach are considered as single-particle cases. The Hölzer and Sommerfeld correlation can be applied to arbitrary shaped particles where the shape of the particle is taken into account through sphericity, and lengthwise and crosswise sphericity:

$$C_D = \frac{8}{\mathrm{Re}} \frac{1}{\sqrt{\Phi_\parallel}} + \frac{16}{\mathrm{Re}} \frac{1}{\sqrt{\Phi}} + \frac{3}{\sqrt{\mathrm{Re}}} \frac{1}{\Phi^{3/4}} + 0.42 \times 10^{0.4(-\log \Phi)^{0.2}} \times \frac{1}{\Phi_\perp} \tag{11}$$

where the particle Reynolds number Re_p is calculated using the expression defined after the Eq. (10). The particle sphericity (Φ), the lengthwise sphericity ($\Phi_\parallel$), and the crosswise sphericity ($\Phi_\perp$) are calculated as:

$$\Phi = \frac{6 V_p^{2/3}}{A_p} \pi^{1/3} \tag{12}$$

$$\Phi_\perp = \frac{A_e}{A_{p,\perp}} \text{ where } A_{p,\perp} = \pi d_p^2 + d_p L_{rod} \sin\theta \tag{13}$$

$$\Phi_\parallel = \frac{2A_e}{A_p - A_{p,\parallel}} \text{ where } A_{p,\parallel} = \pi d_p^2 + d_p L_{rod} \cos\theta \tag{14}$$

where V_p is the volume of the particle, A_p is the surface area of the particle, and A_e is the cross-sectional area of the volume equivalent sphere. For a sphere $\Phi = \Phi_\parallel = \Phi_\perp = 1$.

The multi-particle correlation defined by Sanjeevi and Padding (2020) calculates the drag force experienced by a particle as:

$$\mathbf{F}_D = 3\pi \eta_f d_p \overline{F}_{D,\phi} (\mathbf{v}_f - \mathbf{v}_i) \tag{15}$$

where $\overline{F}_{D,\phi}$ is the average drag (normalised by the drag on an isolated volume equivalent sphere) based on the particle orientation with respect to the fluid flow (ϕ). Sanjeevi et al. showed that the average drag $\overline{F}_D$ for different ϕ follows a sine-square interpolation for individual particles as well as assemblies (Sanjeevi and Padding, 2020; Sanjeevi et al., 2018), where the average drag $\overline{F}_D$ for any ϕ can be calculated as:

$$\overline{F}_{D,\phi} = \overline{F}_{D,\phi=0^\circ} + \left(\overline{F}_{D,\phi=90^\circ} - \overline{F}_{D,\phi=0^\circ}\right) \sin^2 \phi \tag{16}$$

$\overline{F}_{D,\phi=0^\circ}$ and $F_{D,\phi=90^\circ}$ are a function of Re and ϕ:

$$\overline{F}_D(\mathrm{Re}, \epsilon_s) = F_{d,isol} \cdot (1 - \epsilon_s)^2 + F_{\epsilon_s} + F_{\mathrm{Re},\epsilon_s} \tag{17}$$

The corresponding terms are as follows:

$$F_{d,isol}(Re) = C_{d,isol} \frac{\mathrm{Re}}{24} \tag{18}$$

where $C_{d,isol}$ is calculated as proposed by Sanjeevi et al. (2018):

$$C_{d,isol} = \left(\frac{a_1}{\mathrm{Re}} + \frac{a_2}{\mathrm{Re}^{a_3}}\right) \exp(-a_4 \mathrm{Re}) + a_5(1 - \exp(a_4 \mathrm{Re})) \tag{19}$$

where the coefficients ($a_1 \ldots a_5$) for parallel ($\phi = 0^o$) and perpendicular ($\phi = 90^o$) orientation are given in Table 2.

$$F_{\epsilon_s}(\epsilon_s) = a\sqrt{\epsilon_s}(1 - \epsilon_s)^2 + \frac{b\epsilon_s}{(1 - \epsilon_s)^2} \tag{20}$$

$$F_{\mathrm{Re},\epsilon_s}(\mathrm{Re}, \epsilon_s) = \mathrm{Re}^c \epsilon_s^d \left(e(1 - \epsilon_s) + \frac{f{\epsilon_s}^3}{(1 - \epsilon_s)}\right) + g\epsilon_s(1 - \epsilon_s)^2 \mathrm{Re} \tag{21}$$

The coefficients for Eqs. (20) and (21) for parallel and perpendicular orientation are also given in Table 2. Even though the multi-particle correlation takes into account the effect of surrounding particles on the drag force experienced by a particle, sub-grid inhomogeneities such as channeling, which are known to occur in beds of elongated particles at velocities around U_{mf}, are not taken into account by this correlation.

In case of AR-4 particles, next to drag force, lift force and hydrodynamic torque are also considered. Their effect on the fluidization characteristics of AR-4 particles has been studied in our previous work (Mema et al., 2019).

Lift force. *Single-particle lift correlation* The magnitude of the shape induced lift force F_L experienced by an isolated particle is expressed as

$$F_L = \frac{1}{2} C_L \rho_f \frac{\pi}{4} d_p^2 |\mathbf{v}_f - \mathbf{v}_i|^2 \tag{22}$$

where C_L is the lift force coefficient. As the lift force is perpendicular to fluids relative velocity $\mathbf{v}'_{fi} = \mathbf{v}_f - \mathbf{v}_i$ and lies in the plane defined by the particle long axis orientation vector $\mathbf{u}_i$ and $\mathbf{v}'_{fi}$, the lift force magnitude F_L is multiplied by the lift force orientation vector $\hat{\mathbf{e}}_{L_0}$ which is given as

$$\hat{\mathbf{e}}_{L_0} = \frac{\mathbf{u}_i \cdot \mathbf{v}'_{fi}}{|\mathbf{u}_i \cdot \mathbf{v}'_{fi}|} \frac{\left(\mathbf{u}_i \times \mathbf{v}'_{fi}\right) \times \mathbf{v}'_{fi}}{\left|\left|\left(\mathbf{u}_i \times \mathbf{v}'_{fi}\right) \times \mathbf{v}'_{fi}\right|\right|} \tag{23}$$

The resultant lift force experienced by a particle is then expressed as $\mathbf{F}_L = F_L \hat{\mathbf{e}}_{L_0}$.

Table 2
Coefficients for drag force calculation as proposed by Sanjeevi et al. (2018), Sanjeevi and Padding (2020).

	$\overline{F}_D$			$C_{d,isol}$	
Coefficient	$\phi = 0^\circ$	$\phi = 90^\circ$		$\phi = 0^\circ$	$\phi = 90^\circ$
a	2	3	a_1	24.48	31.89
b	11.3	17.2	a_2	3.965	5.519
c	0.69	0.79	a_3	0.41	0.229
d	0.77	3	a_4	0.0005	0.0032
e	0.42	11.12	a_5	0.15	1.089
f	4.84	11.12			
g	0	0.57			

The lift force coefficient is approximated using the correlation by Zastawny et al. (2012)

$$\mathrm{C}_{L,\alpha} = \left(\frac{b_1}{\mathrm{Re}^{b_2}} + \frac{b_3}{\mathrm{Re}^{b_4}}\right) \sin(\alpha)^{b_5 + b_6 \mathrm{Re}^{b_7}} \cos(\alpha)^{b_8 + b_9 \mathrm{Re}^{b_{10}}} \tag{24}$$

Fitting coefficients used for the correlation can be found in Table 3

Multi-particle lift correlation. Sanjeevi and Padding (2020) proposed a simplified calculation for shape induced lift force at different inclination angles ϕ, based on its relation to the normalized drag force. The average lift force $\overline{\mathrm{F}}_L$ (normalised by the drag on an isolated volume equivalent sphere) experienced in a multi-particle system at different ϕ is calculated as:

$$\overline{F}_{L,\phi} = \left(\overline{F}_{D,\phi=90^\circ} - \overline{F}_{D,\phi=0^\circ}\right) \sin\phi \cos\phi \tag{25}$$

The magnitude of multi-particle lift force is calculated as:

$$F_L = 3\pi \eta_f d_p \overline{F}_{L,\phi} |\mathbf{v}_f - \mathbf{v}_i| \tag{26}$$

Hydrodynamic torque. *Single-particle torque correlation.* The magnitude of the hydrodynamic torque on an isolated AR-4 particle is calculated as

$$\mathrm{T}_P = \frac{1}{2} \mathrm{C}_\mathrm{T} \rho_f \frac{\pi}{8} d_p^3 |\mathbf{v}_f - \mathbf{v}_i|^2 \tag{27}$$

where C_T is the torque coefficient. The hydrodynamic torque acts perpendicularly to the plane of particle relative velocity and particle orientation vector. Hence, the torque orientation vector $\hat{\mathbf{e}}_{T_0}$ is given by

$$\hat{\mathbf{e}}_{T_0} = \frac{\mathbf{v}'_{fi} \cdot \mathbf{u}_i}{\left|\mathbf{v}'_{fi} \cdot \mathbf{u}_i\right|} \frac{\mathbf{v}'_{fi} \times \mathbf{u}_i}{\left\|\mathbf{v}'_{fi} \times \mathbf{u}_i\right\|} \tag{28}$$

The resultant torque is then expressed as $\mathbf{T}_p = T_p \hat{\mathbf{e}}_{T_0}$. For approximating the torque coefficient on an isolated particle we have also applied a correlation derived by Zastawny et al. (2012)

Table 3
Coefficients for the lift and torque correlations with the functional form of Zastawny et al. (2012) fitted for spherocylinder particles with aspect ratio of 4 using in-house DNS simulations (Sanjeevi and Padding, 2017; Sanjeevi et al., 2018).

Lift		**Torque**	
Coefficient	Value	Coefficient	Value
b_1	1.884	c_1	−2.283
b_2	0.1324	c_2	−0.01145
b_3	0.001668	c_3	4.09
b_4	−0.8159	c_4	−0.01395
b_5	0.8562	c_5	0.3406
b_6	0.003624	c_6	0.3609
b_7	0.6598	c_7	0.1355
b_8	−0.2621	c_8	0.2356
b_9	0.8021	c_9	0.3612
b_{10}	0.04384	c_{10}	0.1358

Table 4
Coefficients for torque calculation (Eq. (33)) as proposed by Sanjeevi and Padding (2020).

Coefficients	$\mathrm{T}_{\mathrm{Re},\epsilon_s}$
a	0.82
b	1.44
c	1.07
d	5.48
e	0.223

Table 5
Relevant parameters for the CFD-DEM algorithm.

Parameter	Symbol	Value
CFD parameters		
Reactor base	L_x, L_y	0.15 m, 0.15 m
Reactor height	H_z	1.05 m
Number of grid cells	n_x^g, n_y^g, n_z^g	10 × 10 × 70
Grid cell dimensions	$c_x = c_y = c_z$	0.015 m
Time step	t_{CFD}	1×10^{-4} s
Fluid density	ρ_f	1.2 kg/m^3
Fluid viscosity	η_f	$1.568 \cdot 10^{-5}$ Pa · s
DEM parameters		
Time step	t_{DEM}	1×10^{-5} s
Coefficient of friction	μ	0.46
Cofficient of rolling friction	μ_r	0.46
Coefficient of restitution	e	0.43

Table 6
Particle properties.

Particles		
Parameter	AR-1	AR-4
Number of particles	32500	32500
Particle length [L]	-	12 mm
Particle diameter [2R]	5.3 mm	3 mm
Particle density	1442 kg/m^3	1442 kg/m^3
Minimum fluidization velocity [$\mathrm{U_{mf}}$]	1.58 m/s	1.7 m/s

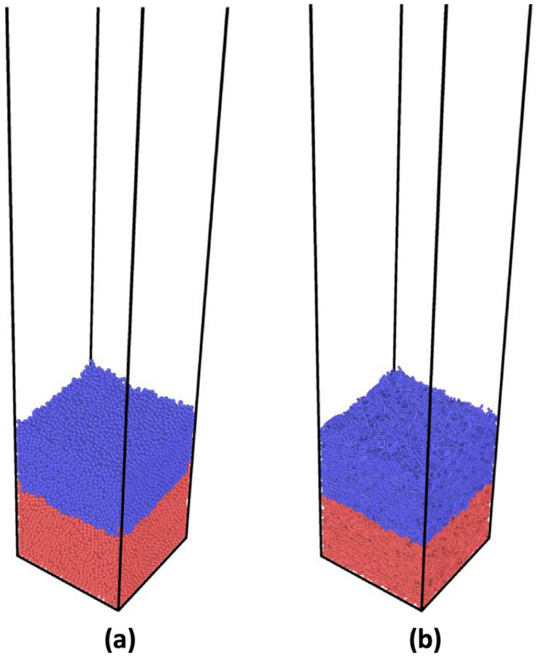

Fig. 1. Initial beds for (a) AR-1 and (b) AR-4 particles.

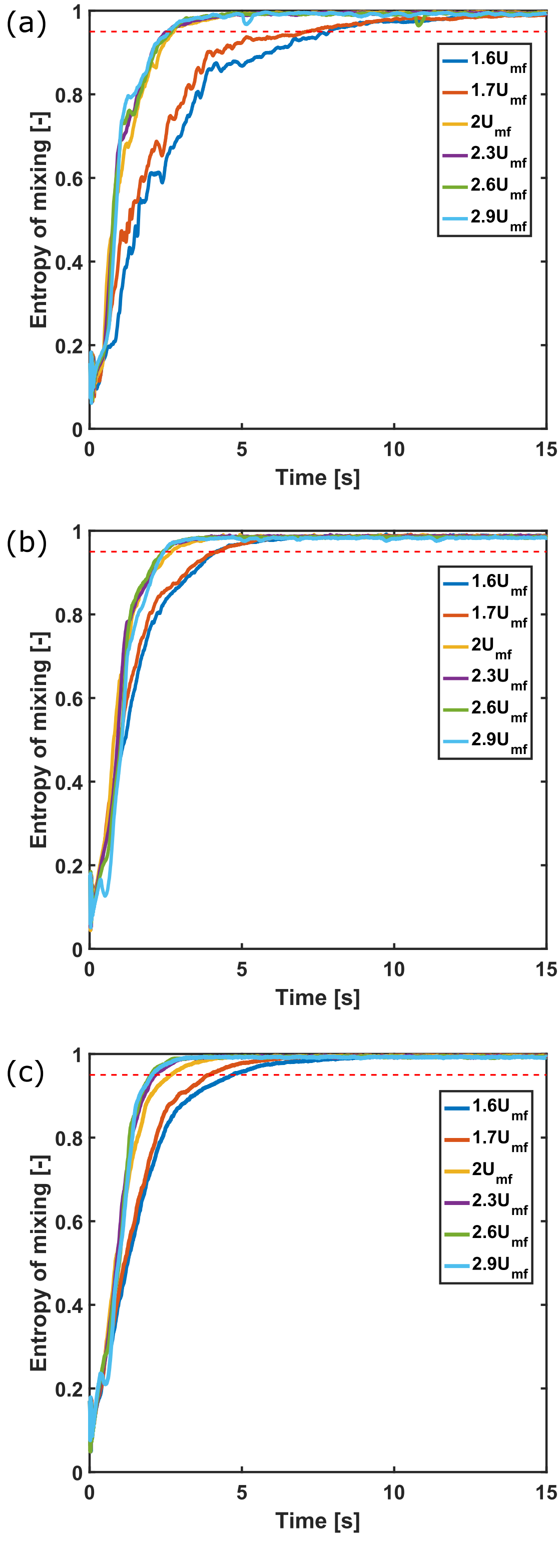

Fig. 2. Mixing entropy as function of time for (a) AR-1 particles, (b) AR-4 (SP) and (c) AR-4 (MP) particles.

$$C_{T,\alpha} = \left(\frac{c_1}{\mathrm{Re}^{c_2}} + \frac{c_3}{\mathrm{Re}^{c_4}}\right) \sin(\alpha)^{c_5 + c_6 \mathrm{Re}^{c_7}} \cos(\alpha)^{c_8^Z + c_9^Z \mathrm{Re}^{c_{10}^Z}} \tag{29}$$

The fitting coefficients used for calculating lift and torque coefficient have been derived by in-house direct numerical simulations (DNS) specifically for AR-4 spherocylindrical particles. More information about the DNS simulations can be found in Sanjeevi and Padding (2017), Sanjeevi et al. (2018). The coefficients used for Zastawny et al. correlations for lift and torque are listed in Table 3

Multi-particle torque correlation. The magnitude of the multi-particle torque proposed by Sanjeevi and Padding (2020) is calculated as:

$$T_P = 2\pi\eta_f d_p^2 \overline{T}_{P,\phi} |\mathbf{v}_f - \mathbf{v}_i| \tag{30}$$

where $\overline{T}_{P,\phi}$ is the average hydrodynamic torque for a multi-particle system, calculated by:

$$\overline{T}_{P,\phi}(\mathrm{Re}, \epsilon_s, \phi) = T_{P,\mathrm{mag}}(\mathrm{Re}, \epsilon_s) \sin\phi \cos\phi \tag{31}$$

with

$$T_{P,\mathrm{mag}}(\mathrm{Re}, \epsilon_s) = T_{p,\mathrm{isol}}(\mathrm{Re}) \cdot (1 - \epsilon_s)^2 + T_{\mathrm{Re},\epsilon_s}(\mathrm{Re}, \epsilon_s) \tag{32}$$

$$T_{\mathrm{Re},\epsilon_s}(\mathrm{Re}, \epsilon_s) = \mathrm{Re}^a \epsilon_s^b \left(c(1 - \epsilon_s) + \frac{d\epsilon_s{}^3}{(1 - \epsilon_s)} \right) + e\epsilon_s(1 - \epsilon_s)^2 \mathrm{Re} \tag{33}$$

Coefficients for Eq. (33) are given in Table 4.

3. Simulation parameters

In this study we used a square fluidized bed which is the same as used in our previous numerical (Mema et al., 2019) and experimental work (Mema et al., 2019). Column dimensions and main CFD-DEM simulation parameters are presented in Table 5. The parameters for particle properties are determined experimentally by Mahajan et al. (2018b) for particles made of alumide, a 3D printing material consisting of a mixture of nylon and aluminum dust. In this work we compare the fluidization mixing characteristics of spherical AR-1 particles to elongated, spherocylindrical AR-4 particles, using single-particle (SP) and multi-particle correlations (MP) (Table 1). The considered particles are volume equivalent to each other as this allows us to compare beds of the same mass and same number of particles which also have relatively similar minimum fluidization velocity. The minimum fluidization velocities were determined experimentally (Mema et al., 2019) and particle properties are listed in Table 6.

In the initial bed, particles are separated by color in two layers, each containing the same number of particles, as shown in Fig. 1. In both layers the particles have identical properties, so the color distinction was made solely for tracking purposes. Horizontal or lateral mixing can be of interest in wide fluidized beds (Oschmann

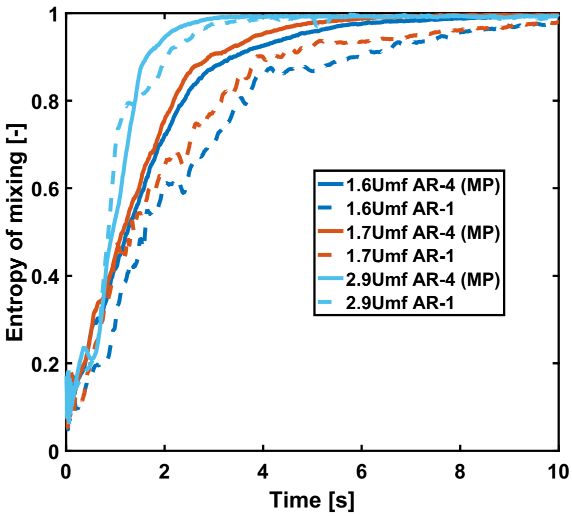

Fig. 3. Comparison of mixing entropy as function of time for AR-1 and AR-1 particles at $1.6U_{mf}$, $1.7U_{mf}$ and $2.9U_{mf}$.

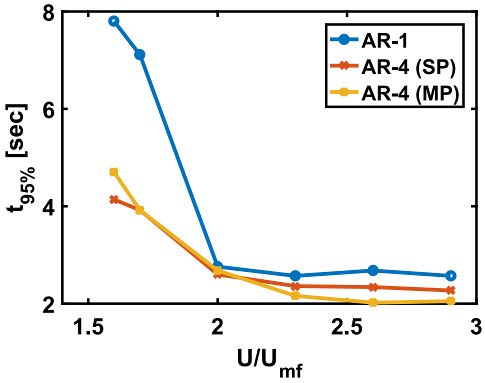

Fig. 4. Mixing time as function of inlet gas velocity for AR-1 and AR-4 particles.

et al., 2014; Oke et al., 2016) However this work refers to vertical mixing due to its higher relevance for tall beds.

Generally, in CFD-DEM simulations of spherical particles the recommended grid size is between $1.6d_p$ and $5d_p$ (Peng et al., 2014). In this work we applied a grid size of $2.83d_p$ which allows us to satisfy standard practice for spherical particles and also have a cell size larger than the length of the AR-4 particle (Mema et al., 2019).

4. Mixing entropy

Literature offers a number of methods to quantify the degree of particle mixing and they all have their advantages and disadvantages (Wen et al., 2015). In fluidized bed investigations two approaches are most popular in recent research: the Lacy mixing index and mixing entropy. For this investigation we decided to focus on mixing entropy as it offers slightly smoother curves and the only parameter that needs to be considered carefully is the choice of the grid size used for measuring the particle fractions (Wen et al., 2015).

Calculating the mixing index, the domain is divided into grid cells indexed by triplets of integers (*i,j,k*). For each cell, the local mixing entropy is calculated using:

$$S(i,j,k) = -x_1(i,j,k)\ln(x_1(i,j,k)) - x_2(i,j,k)\ln(x_2(i,j,k)) \qquad (34)$$

where $x_1(i,j,k)$ and $x_2(i,j,k)$ are number fractions of the colored particles in the cell under investigation.

Local mixing entropies are summed in order to obtain the total normalized mixing entropy (S_{tot}) for each time during the simulation.

$$S_{tot} = \frac{1}{S_0}\sum_{i,j,k} S(i,j,k)\cdot\frac{N_{cell}(i,j,k)}{N} \qquad (35)$$

where S_0 is the maximum entropy of a randomly mixed system, which depends on the ratio of the number of the two types of particles in the system. For the 1:1 ratio used here, we have $S_0 = -\ln 1/2 = \ln 2$. In Eq. (35), we weigh each local mixing entropy with the number of particles $N_{cell}(i,j,k)$ in cell (*i,j,k*) to properly average the total mixing entropy.

When the size of the grid cell used for measuring the fractions is too small, the measurement of the mixing entropy is hampered by statistical noise. Conversely, when the size of the grid cell is too large, the spatial distribution of the particles is ignored. For the dimensions of fluidized bed considered in this work, dividing the domain in coarse grid of 5 × 5 × 35 cells proved to be optimal for accurately determining the mixing entropy.

Mixing time. The mixing entropy gives valuable information on how mixing between particles progresses over time. This also enables us to estimate the mixing time for each case. The normalized mixing entropy varies between values of 0 and 1 for com-

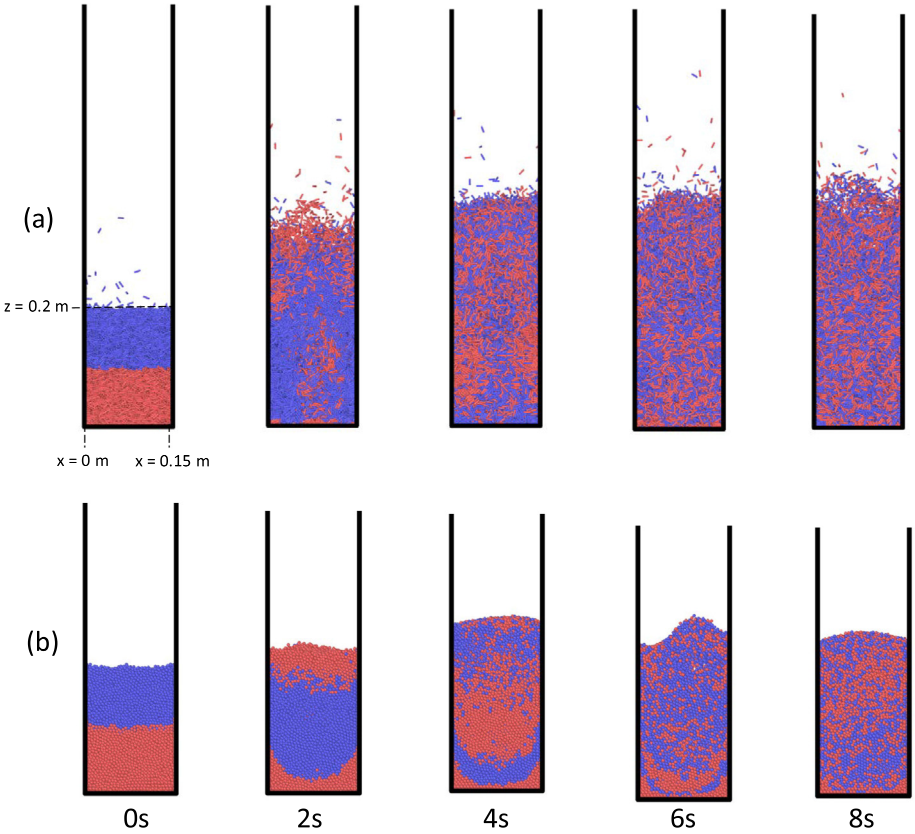

Fig. 5. Visualization of fluidization at different time instants for (a) AR-4 and (b) AR-1 particles at $1.6U_{mf}$.

pletely separated and perfectly mixed systems, respectively. Because in practice perfect mixing is never reached, in this work we use a value of 0.95 for the mixing entropy to define a sufficiently mixed system. The same approach was also applied by Deen et al. (2010). The mixing time $t_{95\%}$ is defined as the time at which the mixing entropy reaches a value of 0.95, as shown by a horizontal dashed line in Fig. 2.

5. Results

In this section we present results on particle mixing in terms of mixing entropy and mixing time. We compare mixing characteristics of AR-1 to AR-4 particles at 6 different gas inlet velocities ($1.6U_{\mathrm{mf}}, 1.7U_{\mathrm{mf}}, 2U_{\mathrm{mf}}, 2.3U_{\mathrm{mf}}, 2.6U_{\mathrm{mf}}$ and $2.9U_{\mathrm{mf}}$). For AR-4 particles we look into the effect of single-particle (SP) and multi-particle (MP) correlations, as well as considering hydrodynamic lift force and torque at 4 gas inlet velocities ($1.6U_{\mathrm{mf}}, 1.7U_{\mathrm{mf}}, 2U_{\mathrm{mf}}$ and $2.9U_{\mathrm{mf}}$). All simulations were run for 20 s which for this size of fluidized bed is enough to reach statistical steady-state (Mema et al., 2019).

5.1. Particle mixing

Fig. 2 shows mixing entropies as a function of time for AR-1 particles and AR-4 particles with single-particle and multi-particle correlations, under the influence of different gas velocities. It can be seen that varying the gas velocity between $1.6U_{\mathrm{mf}}$ and $2U_{\mathrm{mf}}$ leads to a considerable change in mixing entropy. This is particularly the case when changing from $1.6U_{\mathrm{mf}}$ to $1.7U_{\mathrm{mf}}$. However with an increase of gas velocity above $2U_{\mathrm{mf}}$ no additional effect on the evolution of the mixing entropy can be noticed anymore. This can be observed for all considered cases. By comparing the mixing entropy curves for AR-4 particles, it can be seen that using single-particle or multi -particle correlations for hydrodynamic forces does not have a considerable effect on particle mixing. Hovewer, the difference in mixing entropy between AR-1 and AR-4 particles is more evident.

We now make a more quantitative comparison of mixing entropies for AR-1 and AR-4 (MP) particles for the two lower gas velocities $1.6U_{\mathrm{mf}}$ and $1.7U_{\mathrm{mf}}$ and the highest gas velocity $2.9U_{\mathrm{mf}}$, as shown in Fig. 3. Solid lines represent AR-4 particles while dashed lines represent AR-1 particles. Different gas velocities are distinguished by color.

From Fig. 3 clear differences between AR-1 and AR-4 particles can be observed for 1.6 and $1.7U_{\mathrm{mf}}$ where AR-4 particles show considerably higher mixing entropy values and therefore more intensive mixing. This behavior was already observed by Oschmann et al. (2014). However, at the highest considered gas velocity of $2.9U_{\mathrm{mf}}$ the difference between mixing of the two types of particles is becoming negligible.

Condensing the mixing entropy curves into one value as mixing time ($t_{95\%}$), as explained in Section 4, gives more insight in the comparison between AR-1 and AR-4 particles. Fig. 4 shows the time necessary for a fluidized bed to reach a sufficiently mixed state, with a normalized mixing entropy value of 0.95, as a function of gas inlet velocity. Here the difference between considered cases becomes even clearer. At higher gas velocities it can be noticed that even though differences in the mixing time between the two types of particles is getting lower, AR-4 particles continue to show lower mixing times. The effect of gas velocity on the mixing time is considerably higher for for AR-1 particles than for AR-4 particles in the range between $1.6U_{\mathrm{mf}}$ and $2U_{\mathrm{mf}}$. Choosing between single-particle or multi-particle correlations for AR-4 particle has only a slight effect on the mixing time. However, it can be noticed that MP correlations increase the difference in mixing time between AR-1 and AR-4 particle at higher gas velocities ($> 2U_{\mathrm{mf}}$).

The previous work by Oschmann et al. (2014) already reported less intensive mixing for spherical particles and for particles of lower aspect ratio. However the physical reason for this difference is still not clear. Figs. 5 and 6 show a visualization of fluidization of AR-1 and AR-4 particles at the lowest ($1.6U_{\mathrm{mf}}$) and highest ($2.9U_{\mathrm{mf}}$) gas velocities at different time instances. From Fig. 5 it is already visually clear that AR-1 particles show considerably less intensive mixing after a given amount of time. It seems that for the same gas velocity (U/U_{mf}), AR-4 particles have a higher bed expansion with more vigorous mixing, while AR-1 particles show distinct layers of the same particle colors. The reason for this can be that large (Geldart D type) AR-4 particles show more intensive turbulent fluidization behavior than volume equivalent AR-1 particles for the same gas velocity (Mema et al., 2020). In our previous experimental investigation (Mema et al., 2020), we have shown that while AR-1 particles remain in a constant slugging regime, AR-4 particles

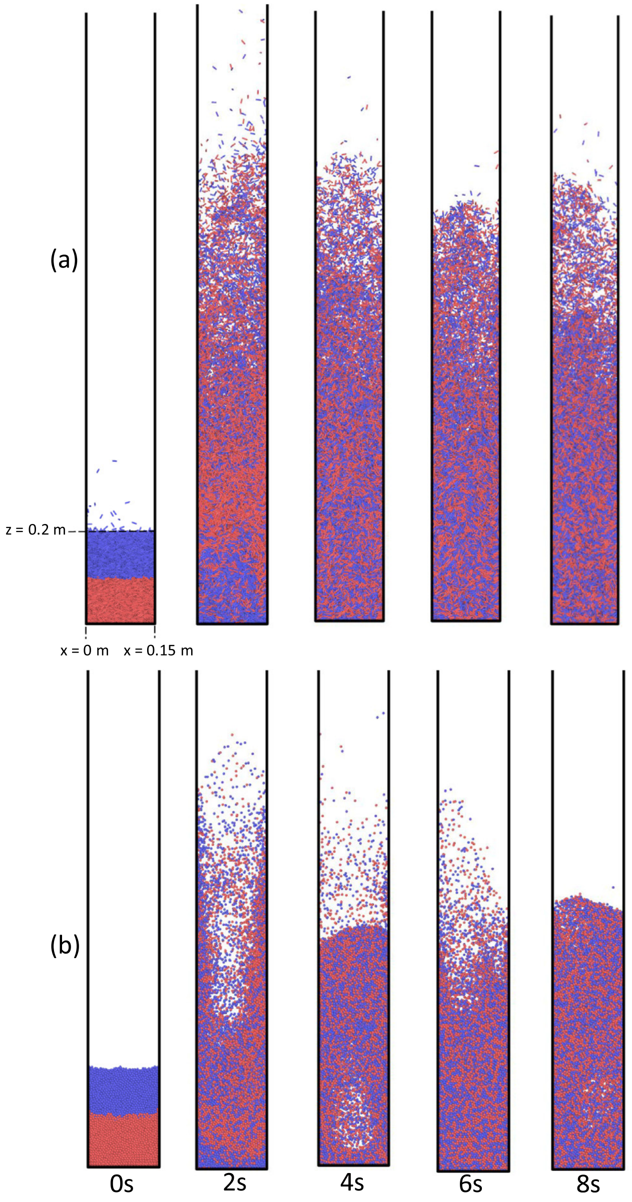

Fig. 6. Visualization of fluidization at different time instants for (a) AR-4 and (b) AR-1 particles $2.9U_{\mathrm{mf}}$.

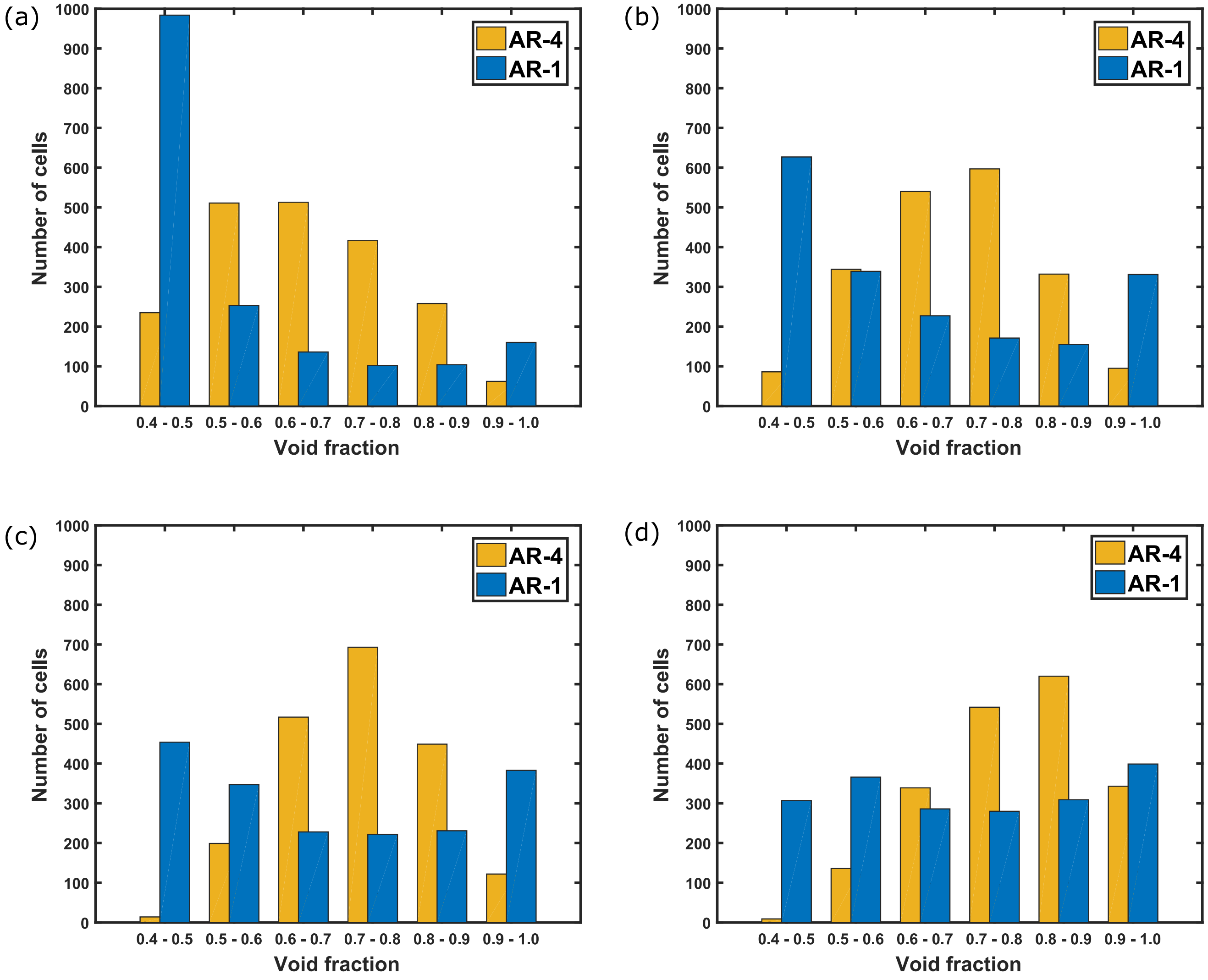

Fig. 7. Histogram of void fractions for cells below z = 0.3 m (total of 2000 cells) for AR-1 and AR-4 (MP) particles at (a) $1.6U_{mf}$, (b) $2U_{mf}$, (c) $2.3U_{mf}$ and (d) $2.9U_{mf}$.

show more turbulent behavior and periodically switch between slugging and turbulent fluidization.

As the bubbles are main carriers responsible for particle mixing in fluidized beds and the main mixing occurs in the bubble wake (Kunii, 2013; Rowe and Nienow, 1976), it is expected that fluidized beds with flat nose, raining slugs, that are characteristic for large Geldart D particles (Kunii, 2013), cannot lead to as effective particle mixing as bubbling or turbulent fluidized beds.

From Fig. 6 it can be observed that at the highest gas velocity of 2.9Umf, AR-1 particles are also in a much more turbulent fluidizing regime, more similar to AR-4 particles. Fig. 7 gives more insight in the void fraction distribution for the lower part of the bed ($z < 0.3$ m), where for all gas velocities we expect to be in the dense part of the fluidized bed. As void fractions between 0.4 and 0.5 respond to densely packed beds, and between 0.9 and 1.0 to cells with barely any particles in them, from Fig. 7 it can be seen that AR-1 particles generally show a much more binary distribution of void fractions (i.e. either very dense or very dilute) compared to AR-4 particles which show a much wider distributions in the middle range of void fractions. At the low gas velocity of $1.6U_{mf}$, AR-1 particles are still densely packed, with individual bubbles passing trough the bed and carrying out the mixing. While for AR-4 particles, even at such low gas velocities, the particles are more suspended in the gas flow, which can lead to faster mixing.

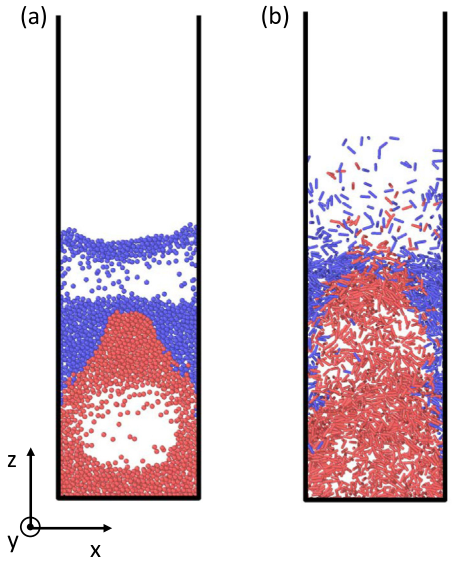

Fig. 8. Snapshots of bubble formations for (a) AR-1 and (b) AR-4 (MP) particles at $1.7U_{mf}$ in the middle intersection of the bed ($0.07 \text{ m} \leqslant y \leqslant 0.08$ m).

This is more visually evident from the snapshots in Fig. 8. It can be seen that in the case of AR-1 particles, bubbles are clearly formed and the boundary between densely packed particles and gas bubbles is clearly visible. In the case of AR-4 particles, no clear bubbles are formed and particles are generally more suspended in the gas flow.

From Fig. 7 it can be seen that with the increase of gas velocity, there is an increase in the intermediate range of void fractions for AR-1 particles, however it still remains lower than in the case of AR-4 particles. AR-1 particles also show a higher peak at void fractions in the range 0.9–1.0, which still suggests that clear bubbles (or slugs) are passing through the bed. With the increase of gas velocity, the distribution of void fractions for AR-4 particles moves to the values corresponding to more dilute cells. Overall, these observations can explain the faster mixing times we observe in the case of AR-4 particles.

In our previous work (Mema et al., 2020) we already started to see indications of transition to a turbulent fluidization regime for spherical particles at a gas velocity of $1.9U_{mf}$, which can explain the large drop in mixing time for AR-1 particles at $2U_{mf}$. This is consistent with our observation that above $2U_{mf}$ we see negligible difference between AR-1 and AR-4 particles, as both are operating in the turbulent fluidizing regime.

5.2. Effect of hydrodynamic lift force and torque on mixing characteristics of elongated particles

So far, most numerical works have neglected the effect of hydrodynamic lift and torque on fluidizaton of non-spherical particles. However, in case of elongated particles these forces have considerable effect on the average particle orientation and velocity distribution (Mema et al., 2019). In this section we investigate the effect of considering lift and torque on mixing behavior of AR-4 particles. Fig. 9 compares the mixing entropy and the mixing times for cases with only multi-particle drag force considered to cases where all hydrodynamic forces (using multi-particle correlations) are considered, for different gas velocities.

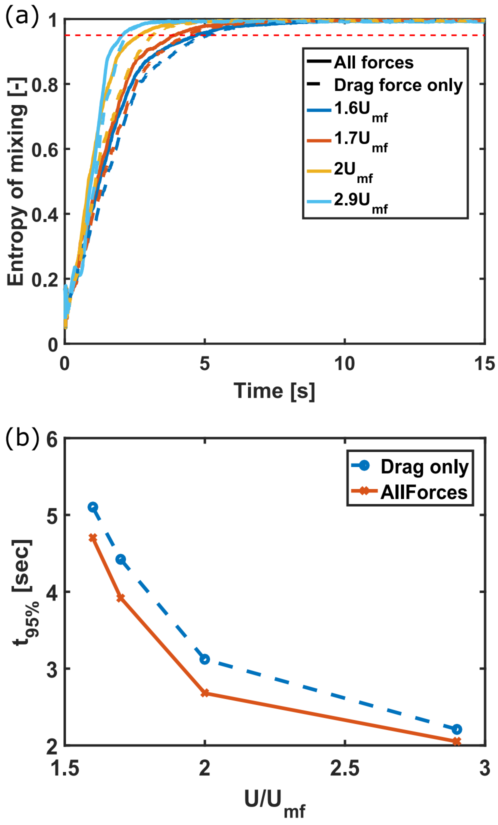

Fig. 9. Effects of considering hydrodynamic lift and torque on (a) mixing entropy and (b) mixing time for AR-4 (MP) particles.

From Fig. 9 (a) it can be observed that cases with all hydrodynamic forces considered (full lines in Fig. 9) show higher mixing entropies than cases where only the drag force is considered (dashed lines in Fig. 9). This difference is diminishing with increasing gas velocity.

Similar behavior can be seen in the mixing time (Fig. 9 (b)) where for $1.6U_{mf}$, $1.7U_{mf}$ and $2U_{mf}$ simulations with lift and torque show lower mixing times. At the highest velocity of $2.9U_{mf}$ both cases have almost identical mixing times. The fact that after $2U_{mf}$ we do not see any effect of varying gas velocity (Figs. 3 and 4) or hydrodynamic forces on mixing properties indicates that we have reached a terminal mixing time and that for the considered properties of the fluidized bed (column and particle properties) it is not possible to achieve faster mixing. From the presented results it can be assumed that the terminal mixing times for AR-1 and AR-4 particles in the fluidzed bed considered in this work are around 2.6 and 2.3 s, respectively.

The effect of including lift and torque on mixing time can be attributed mainly to the lift force. Including hydrodynamic lift force leads to an increase in average particle velocity in the vertical z-direction (Mema et al., 2019). As can be seen from the previous Section 5.1, increasing gas velocity leads to faster and more intensive mixing.

6. Conclusion

In this work, we applied CFD-DEM simulations to compare mixing behavior of spherical (AR-1) particles to elongated spherocylinders (AR-4) in a fluidized bed and to investigate the effect of novel multi-particle correlations for hydrodynamic forces and torque (Sanjeevi and Padding, 2020) compared to widely used single-particle correlations. Spherical (AR-1) particles show less vigorous mixing than AR-4 particles and have higher mixing times. The largest difference can be seen for gas velocities up to $2U_{mf}$. At higher gas velocities, even though AR-1 particles still show longer mixing times, differences can be considered negligible. This indicates that between $2U_{mf}$ and $2.3U_{mf}$ the fluidized bed already reaches a terminal mixing velocity and it is not possible to achieve faster mixing times for the given fluidized bed properties. More vigorous mixing for AR-4 particles can be explained by the more turbulent fluidization. These observations are characteristic of tall and narrow beds with coarse particles. Different conclusions are possible for shallower beds with lower bed height to column diameter ratios.

Applying multi-particle correlations for hydrodynamic forces and torque does not have a large effect on particle mixing times. It can be noted that the mixing times for cases with multi-particle correlations at higher gas velocities ($> 2.3U_{mf}$) have slightly lower mixing times compared to the cases with single particle correlations, however this effects can be seen as marginal.

Including hydrodynamic lift and torque has an effect on mixing properties of AR-4 particles and leads to somewhat faster mixing times. The main cause for faster mixing times can be seen in the effect of lift force which increases the particle average velocity in the vertical direction.

CRediT authorship contribution statement

Ivan Mema: Investigation, Formal analysis, Writing - original draft, Writing - review & editing, Visualization. **Johan T. Padding:** Supervision, Project administration, Funding acquisition.

Declaration of Competing Interest

The authors declare that they have no known competing financial interests or personal relationships that could have appeared to influence the work reported in this paper.

Acknowledgments

The authors thank the European Research Council for its financial support under its consolidator grant scheme, contract No. 615096 (NonSphereFlow).

The work has been made possible by a grant for computation time, project number 2019.013, financed by the Netherlands Organisation for Scientific Research (NWO).

References

Banaei, M., Deen, N., van Sint Annaland, M., Kuipers, J., 2018. Particle mixing rates using the two-fluid model. Particuology 36, 13–26. https://doi.org/10.1016/j.partic.2017.01.009.

Cundall, P.A., Strack, O.D.L., 1979. A discrete numerical model for granular assemblies. Géotechnique 29 (1), 47–65. https://doi.org/10.1680/geot.1979.29.1.47.

Deen, N.G., Willem, G., Sander, G., Kuipers, J.A.M., 2010. Numerical analysis of solids mixing in pressurized fluidized beds. Ind. Eng. Chem. Res. 49 (11), 5246–5253. https://doi.org/10.1021/ie9014843.

Felice, R.D., 1994. The voidage function for fluid-particle interaction systems. Int. J. Multiph. Flow 20 (1), 153–159.

Hölzer, A., Sommerfeld, M., 2008. New simple correlation formula for the drag coefficient of non-spherical particles. Powder Technol. 184 (3), 361–365. https://doi.org/10.1016/j.powtec.2007.08.021.

Kloss, C., Goniva, C., Hager, A., Amberger, S., Pirker, S., 2012. Models, algorithms and validation for opensource DEM and CFD-DEM, Progress in Computational Fluid Dynamics. Int. J. 12 (2/3), 140. https://doi.org/10.1504/pcfd.2012.047457.

Kunii, O.L.D., 2013. Fluidization Engineering. Elsevier Science.

Lu, G., Third, J., Müller, C., 2015. Discrete element models for non-spherical particle systems: From theoretical developments to applications. Chem. Eng. Sci. 127, 425–465. https://doi.org/10.1016/j.ces.2014.11.050.

Ma, H., Zhao, Y., 2018. CFD-DEM investigation of the fluidization of binary mixtures containing rod-like particles and spherical particles in a fluidized bed. Powder Technol. 336, 533–545. https://doi.org/10.1016/j.powtec.2018.06.034.

Mahajan, V.V., Nijssen, T.M., Kuipers, J., Padding, J.T., 2018a. Non-spherical particles in a pseudo-2d fluidised bed: Modelling study. Chem. Eng. Sci. 192, 1105–1123. https://doi.org/10.1016/j.ces.2018.08.041.

Mahajan, V.V., Padding, J.T., Nijssen, T.M.J., Buist, K.A., Kuipers, J.A.M., 2018b. Nonspherical particles in a pseudo-2d fluidized bed: Experimental study. AIChE J. 64 (5), 1573–1590. https://doi.org/10.1002/aic.16078.

Mema, I., Padding, J., 2020. Fluidization of elongated particles - effect of multi-particle correlations for drag, lift and torque in CFD-DEM. doi:10.22541/au.159234121.14221968.

Mema, I., Mahajan, V.V., Fitzgerald, B.W., Padding, J.T., 2019. Effect of lift force and hydrodynamic torque on fluidisation of non-spherical particles. Chem. Eng. Sci. 195, 642–656. https://doi.org/10.1016/j.ces.2018.10.009.

Mema, I., Buist, K.A., Kuipers, J.H., Padding, J.T., 2019. Fluidization of spherical versus elongated particles: Experimental investigation using magnetic particle tracking. AIChE J. doi:10.1002/aic.16895.

Mema, I., Wagner, E.C., van Ommen, J.R., Padding, J.T., 2020. Fluidization of spherical versus elongated particles - experimental investigation using x-ray tomography. Chem. Eng. J., 125203 https://doi.org/10.1016/j.cej.2020.125203.

Oke, O., van Wachem, B., Mazzei, L., 2016. Lateral solid mixing in gas-fluidized beds: CFD and DEM studies. Chem. Eng. Res. Des. 114, 148–161. https://doi.org/10.1016/j.cherd.2016.08.014.

Oschmann, T., Hold, J., Kruggel-Emden, H., 2014. Numerical investigation of mixing and orientation of non-spherical particles in a model type fluidized bed. Powder Technol. 258, 304–323. https://doi.org/10.1016/j.powtec.2014.03.046.

Peeler, J., Huang, J., 1989. Segregation of wide size range particle mixtures in fluidized beds. Chem. Eng. Sci. 44 (5), 1113–1119. https://doi.org/10.1016/0009-2509(89)87010-1.

Peng, Z., Doroodchi, E., Luo, C., Moghtaderi, B., 2014. Influence of void fraction calculation on fidelity of CFD-DEM simulation of gas-solid bubbling fluidized beds. AIChE J. 60 (6), 2000–2018. https://doi.org/10.1002/aic.14421.

Rhodes, M., Wang, X., Nguyen, M., Stewart, P., Liffman, K., 2001. Study of mixing in gas-fluidized beds using a DEM model. Chem. Eng. Sci. 56 (8), 2859–2866. https://doi.org/10.1016/s0009-2509(00)00524-8.

Rowe, P., Nienow, A., 1976. Particle mixing and segregation in gas fluidised beds. a review. Powder Technol. 15 (2), 141–147. https://doi.org/10.1016/0032-5910(76)80042-3.

Sanjeevi, S.K.P., Padding, J.T., 2017. On the orientational dependence of drag experienced by spheroids. J. Fluid Mech. 820.

Sanjeevi, S.K.P., Padding, J.T., 2020. Hydrodynamic forces on monodisperse assemblies of axisymmetric elongated particles: Orientation and voidage effects. AIChE J. 66(6). doi:10.1002/aic.16951.

Sanjeevi, S.K.P., Kuipers, J.A.M., Padding, J.T., 2018. Drag, lift and torque correlations for non-spherical particles from stokes limit to high reynolds numbers. J. Fluid Mech.

Shen, L., Zhang, M., Xu, Y., 1995. Solids mixing in fluidized beds. Powder Technol. 84 (3), 207–212. https://doi.org/10.1016/0032-5910(95)02994-d.

Shi, Y.F., Fan, L.T., 1984. Lateral mixing of solids in batch gas-solids fluidized beds. Ind. Eng. Chem. Process Des. Develop. 23 (2), 337–341. https://doi.org/10.1021/i200025a026.

Shrestha, S., Kuang, S., Yu, A., Zhou, Z., 2020. Orientation of spheroidal particles in single jet bubbling fluidized beds. Powder Technol. 361, 363–373. https://doi.org/10.1016/j.powtec.2019.07.095.

Thiel, W.J., Potter, O.E., 1978. The mixing of solids in slugging gas fluidized beds. AIChE J. 24 (4), 561–569. https://doi.org/10.1002/aic.690240402.

Vega, C., Lago, S., 1994. A fast algorithm to evaluate the shortest distance between rods. Comput. Chem. 18 (1), 55–59. https://doi.org/10.1016/0097-8485(94)80023-5.

Vollmari, K., Jasevičius, R., Kruggel-Emden, H., 2016. Experimental and numerical study of fluidization and pressure drop of spherical and non-spherical particles in a model scale fluidized bed. Powder Technol. 291, 506–521. https://doi.org/10.1016/j.powtec.2015.11.045.

Wen, Y., Liu, M., Liu, B., Shao, Y., 2015. Comparative study on the characterization method of particle mixing index using DEM method. Proc. Eng. 102, 1630–1642. https://doi.org/10.1016/j.proeng.2015.01.299.

Zastawny, M., Mallouppas, G., Zhao, F., van Wachem, B., 2012. Derivation of drag and lift force and torque coefficients for non-spherical particles in flows. Int. J. Multiph. Flow 39, 227–239. https://doi.org/10.1016/j.ijmultiphaseflow.2011.09.004.

Zhong, W., Yu, A., Liu, X., Tong, Z., Zhang, H., 2016. DEM/CFD-DEM modelling of non-spherical particulate systems: Theoretical developments and applications. Powder Technol. 302, 108–152. https://doi.org/10.1016/j.powtec.2016.07.010.